Paired organic matter and pyrite $\delta^{34}S$ records reveal mechanisms of carbon, sulfur, and iron cycle disruption during Ocean Anoxic Event 2

Morgan Reed Raven[*a,b], David A. Fike [b], Alexander S. Bradley [b]; Maya L. Gomes [c], Jeremy D. Owens [d], Samuel A. Webb [e]

[a] *Dept. of Earth Sciences, University of California, Santa Barbara, CA 93130 USA*
[b] *Dept. of Earth and Planetary Sciences, Washington University in St Louis, MO 63130*
[c] *Dept. of Earth and Planetary Sciences, Johns Hopkins University, Baltimore, MD 21218*
[d] *Dept. of Earth, Ocean, and Atmospheric Science, Florida State University, Tallahassee, FL 32306*
[e] *Stanford Synchrotron Radiation Lightsource, Stanford University, Menlo Park, CA, 94025*
* = *corresponding author, raven@ucsb.edu*

Abstract

The sulfur (S) isotope composition of pyrite in the sedimentary record has played an important part in our understanding of the evolution of biogeochemical cycles throughout Earth history. However, the kinetics of pyritization are complex and depend strongly on the reactivity and mineralogy of available iron. As a second major sink for sulfide in anoxic sediments, organic matter (OM) provides essential context for reconstructing the distribution and isotopic composition of environmental sulfide. To first order, roughly parallel pyrite and OM $\delta^{34}S$ profiles reflect changes in sulfide, while independent patterns require alternative explanations, including changes in iron availability or OM characteristics. We apply this framework to Ocean Anoxic Event 2 (OAE-2, ~94 Mya), a period of enhanced burial of reduced C and S (in OM and pyrite) that has been associated with an expansion of reducing marine conditions. We present paired S-isotope records for pyrite and OM along with profiles of OM S:C ratio and S redox speciation from four well-characterized lithologic sections with a range of depositional environments (Pont d'Issole, Cismon, Tarfaya Basin, and Demerara Rise) to reconstruct both local redox structure and global mechanisms impacting the C, S and Fe cycles around OAE-2.

OM sulfurization appears to be a major control on OM preservation at all four sites. Similar to modern anoxic environments, there is a positive correlation between OM S:C ratios and TOC concentrations for sites with more reducing conditions, implying a link between OM sulfurization and burial. At consistently anoxic sites like Tarfaya Basin and Demerara Rise, strongly sulfurized OM with a consistent S redox speciation and S-isotope composition most likely formed rapidly in sinking particles before, during, and after OAE-2. Particle-

hosted OM sulfurization may therefore have been a central mechanism facilitating the massive burial of OM in anoxic environments during this and other periods of enhanced global carbon burial. At the same time, a nearly 25‰ negative shift in the $\delta^{34}S$ values of pyrite – but not OM – occurs at multiple, globally distributed sites prior to the onset of OAE-2, indicating slower pyritization reactions that likely reflect changes in iron delivery due to expanding regional or global anoxia. The combination of pyrite and organic S isotopes thus provides novel constraints on the interwoven cycles of carbon, iron, and sulfur across a major carbon cycle perturbation.

1. Introduction

Ocean Anoxic Event 2 (OAE-2, also termed the Cenomanian–Turonian Boundary Event) was a period of dynamic changes in the global carbon cycle in the Cretaceous (~94 million years ago, Mya) during which a large portion of the global ocean experienced anoxia (Ostrander et al., 2017) and associated biological turnover (Keller et al., 2008 and refs therein). Expanded euxinia at the onset of the event contributed to the preservation of extraordinary amounts of organic matter (OM) in marine sediments, equivalent to roughly a 60 to 80% increase in the global organic carbon burial flux maintained for ~500,000 years (Owens et al., 2013; 2018; Sageman et al., 2006). This burst of ^{13}C-depleted OM preservation generated the characteristic positive C-isotope excursion for OAE-2 and substantially drew down atmospheric CO_2 (Jarvis et al., 2011). OM sulfurization can enhance the preservation of total organic carbon (TOC) under anoxic conditions (Boussafir et al., 1995) and has been described in TOC–rich (>10 wt%) OAE-2 shales (Hetzel et al., 2009; Kolonic et al., 2002) as well as in interbedded carbonates and marly shales with more

moderate (0.2–3 wt%) TOC (Raven et al., 2018). Still, it remains difficult to quantify the impact of sulfurization on OM preservation under different environmental conditions, much less to extrapolate to global fluxes of reduced sulfur and carbon burial or to estimate how those fluxes might change before, during, and after OAE-2.

Primary considerations for determining the significance of sulfurization for TOC burial are the rates and locations of S cycling in the environment. Two distinct timescales of sulfurization reactions occur in modern environments: gradual sulfurization reactions between bisulfide (HS^-) and relatively recalcitrant OM occur over thousands of years under strongly reducing conditions (Werne et al., 2000), and rapid sulfurization reactions between polysulfides (S_x^{2-}) and relatively fresh, labile OM occur on timescales of days near dynamic redox interfaces, for example in sinking marine particles (Raven et al., 2016a). Rapid sulfurization has the potential to have a much more dramatic impact on TOC burial because it can compete with microbial heterotrophy and preserve part of the relatively large pool of fresh OM sinking out of the surface ocean (Raven et al., 2018). Still, particle-hosted OM sulfurization has not been explicitly considered in analyses of TOC and sulfur burial during periods of expanded oceanic anoxia like OAE-2.

Sulfur–isotope ratios (expressed as $\delta^{34}S$ values) are powerful tools for reconstructing the sources of sulfide in the environment as well as its various potential sinks, including reoxidation or precipitation as either abiogenic organic S or pyrite (FeS_2). Near the onset of OAE-2, previously published S-isotope profiles of pyrite from multiple sites show intriguing shifts toward ^{34}S-depleted values that have been interpreted in terms of changing

84 marine sulfate concentrations (Adams et al., 2010), local chemocline position (Gomes et
85 al., 2016), and the extent of oxidative microbial sulfur cycling (Hetzel et al., 2009; Kolonic
86 et al., 2002). Although each of these hypotheses invoke changes in the distribution or $\delta^{34}S$
87 value of sulfide in the environment, OAE-2 is also associated with major changes in iron
88 cycling due to inputs from active rifting and volcanism (Owens et al., 2012), which could
89 also impact pyrite $\delta^{34}S$ values via changes in iron distributions and mineralogy. If changes
90 in the distribution or isotopic composition of sulfide are driving the shift in pyrite $\delta^{34}S$
91 values near the onset of OAE-2, we should see parallel behavior in the $\delta^{34}S$ values of
92 sulfurized OM and pyrite. If not, changes in pyrite $\delta^{34}S$ values may instead reflect changes
93 in the quantity and/or speciation of locally available iron at this time, which could impact
94 the mechanism and timing of pyrite formation in the environment.

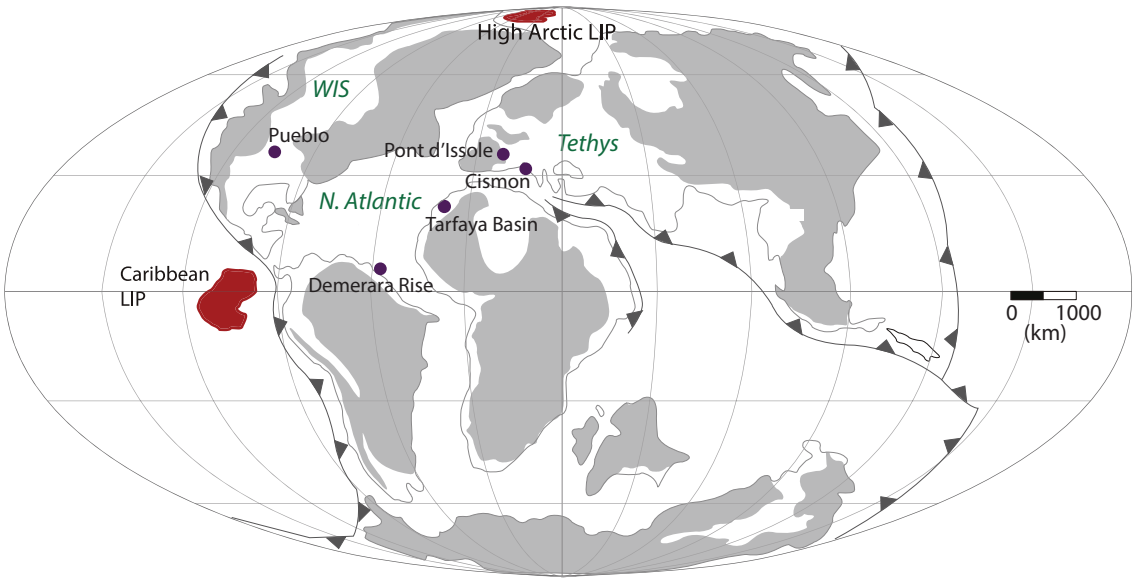

95

96 **Fig. 1 Paleo-geography of study sites during OAE-2.** Map is modified from du Vivier
97 et al. (2014) with study sections marked by purple circles. Locations of Large Igneous
98 Provinces (LIP) are also shown in red.

99

100 To distinguish among these possible drivers of S-isotope variability, we present paired
101 pyrite and OM $\delta^{34}S$ records alongside OM S speciation data for four OAE-2 sections
102 located in different regions of the Tethys and proto–North Atlantic Oceans (Fig. 1). Results
103 for organic S from Pont d'Issole were previously published (Raven et al., 2018); all other
104 data are new to this study. Our results indicate that the strong negative shift in pyrite $\delta^{34}S$
105 values from globally dispersed sites likely reflects a change in the quantity or speciation of
106 iron delivery to these locations. We also find evidence for a generalizable relationship
107 between sulfurization intensity and OM preservation in sediments, which implies that OM
108 sulfurization can be a primary driver of changes in C burial during OAE-2 and throughout
109 the Phanerozoic.

110

111 **2. Brief Methods**

112 Samples were prepared from previously sampled sections (see descriptions in Results) by
113 sequential extraction (Canfield et al., 1986; Raven et al., 2018), as detailed in the
114 Supplementary Information. Powdered rock samples were washed with deionized water,
115 lyophilized, and microwave–extracted to remove organic-solvent soluble S, including any
116 elemental S. Solids were weighed before and after acidification to estimate carbonate
117 mineral ('carbonate') abundance. Pyrite in the carbonate-free sediments was extracted by
118 treatment with hot chromium (II) chloride solution and the released sulfide, which we refer
119 to as 'pyrite', was trapped as ZnS. Washed ZnS solids were oxidized to sulfate, quantified
120 by ion chromatography, and precipitated as $BaSO_4$ for S-isotope analysis. Remaining
121 solids after chromium reduction are considered 'organic S'. All C- and S-isotope ratio

122 measurements were made by combustion EA-IRMS at Washington University in St Louis
123 and are reported in per mil (‰) units relative to VPDB and VCDT, respectively (see
124 Supplementary Information for analytical details). Error bars on Figures (±0.5‰ for $\delta^{34}S$
125 and ±0.2‰ for $\delta^{13}C$) represent typical standard deviations of results for external replicates
126 (separately processed sample splits; n≥3). To determine the bonding environment of
127 organic S, extracted sediments were analyzed by x-ray absorption spectroscopy on
128 beamline 14–3 at the Stanford Synchrotron Radiation Lightsource (SSRL) at the SLAC
129 National Accelerator Laboratory (see Supplementary Information).
130
131 **3. Study Sites and Results**

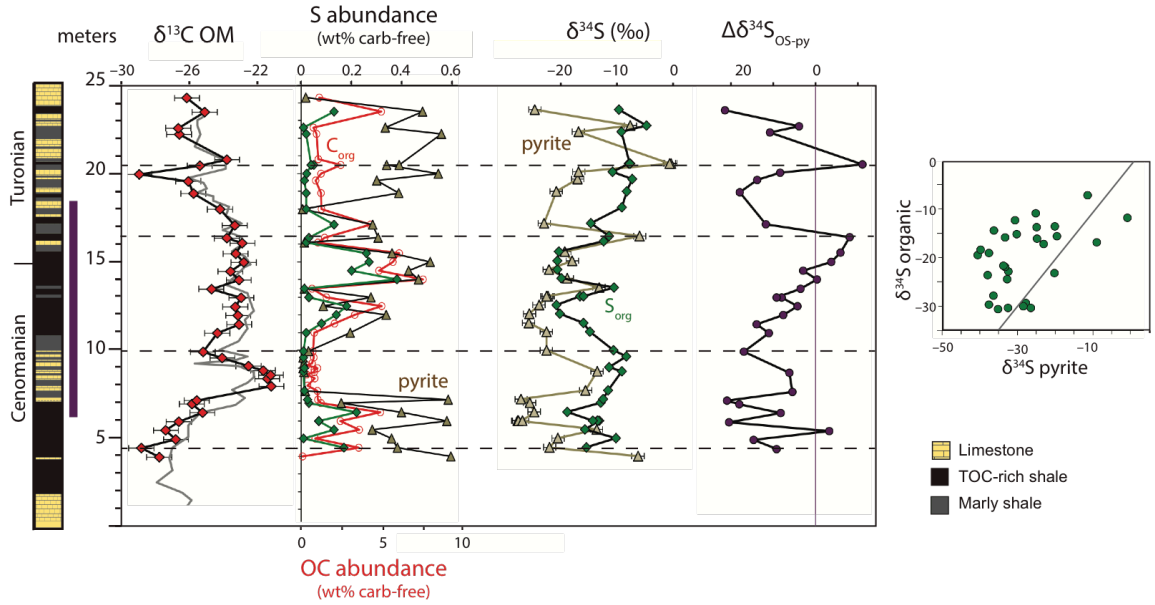

132
133 **Fig. 2 Pont d'Issole record.** The purple bar at left represents the interpreted duration of
134 OAE-2 based on the C-isotope excursion. The grey line for $\delta^{13}C_{OM}$ is from Jarvis et al.
135 (2011), and lithology is from Gomes et al. (2016). Dashed horizontal lines are intended as

136 visual aids to highlight patterns in the records. Vertical purple line for $\Delta\delta^{34}S_{OS\text{-}py}$ shows
137 $\delta^{34}S_{pyrite} = \delta^{34}S_{OS}$. Grey line in the right-hand panel shows a 1:1 line.
138
139 The Pont d'Issole section was deposited in a subsiding basin within the northern Tethys
140 Ocean (~30°N, Fig. 1) in several hundred meters of water depth with an average
141 sedimentation rate of roughly 2.4 cm/yr (based on a 12-m-thick C-isotope excursion
142 spanning ~500 kyr; Jarvis et al., 2011). Samples were collected at outcrop in 2011. A
143 selection of mostly OM-lean carbonates from this section were analyzed previously for S-
144 isotopes in pyrite and carbonate-associated sulfate (Gomes et al., 2016). The Pont d'Issole
145 section is characterized by recurrent shifts in lithology and OM concentration between
146 relatively TOC-lean (<0.2 wt%) limestones and relatively TOC-rich (>1.0 wt%) shales and
147 marly shales. Our pyrite $\delta^{34}S$ profile from Pont d'Issole (Fig. 2) has many similarities to
148 the published OM $\delta^{34}S$ profile (Raven et al., 2018), with comparable shifts toward lower
149 $\delta^{34}S$ values in shales before and during the OAE-2 C-isotope excursion. There are also
150 instances, however, where the S-isotope composition of pyrite behaves independently from
151 that of OM: at 5.5 m and 20.5 m, for example, pyrite is locally strongly ^{34}S-enriched
152 without any parallel excursion in OM $\delta^{34}S$. Additionally, the $\delta^{34}S$ offset between pyrite
153 and organic matter (Fig. 2, $\Delta\delta^{34}S_{OS\text{-}py}$) decreases systematically across the duration of the
154 C-isotope excursion from 17.4‰, a large but not unusual ^{34}S-enrichment for OM relative
155 to pyrite, to –7.9‰, meaning that the normal relationship between pyrite and OM $\delta^{34}S$
156 values is reversed, with OM more ^{34}S-depleted than pyrite (Anderson and Pratt, 1995).
157 Illustrating the variability in $\Delta\delta^{34}S_{OS\text{-}py}$ at Pont d'Issole, OM and pyrite $\delta^{34}S$ values show
158 significant spread around and to the left of the 1:1 line in the cross-plot in Fig. 2.

159

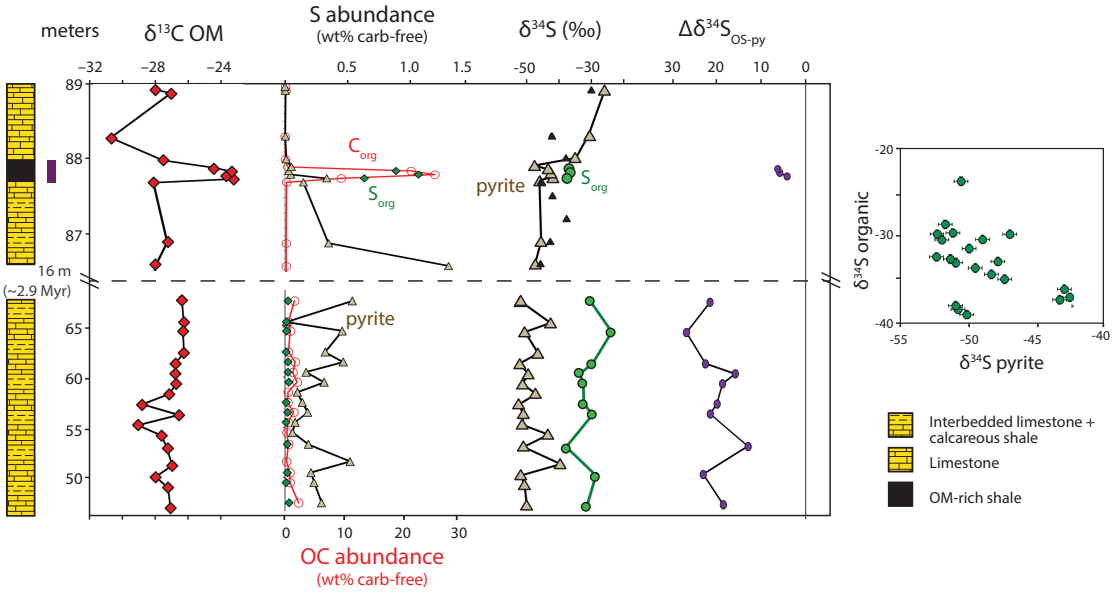

160

161 **Fig. 3 Cismon record.** The purple bar at left represents the interpreted duration of OAE-
162 2 based on the C-isotope excursion. The horizontal dashed line indicates a 16-m gap in the
163 vertical profile comprising very TOC-lean carbonates; note different scales for the upper
164 and lower panels. The duration of this gap is ~2.9 Myr based on foraminiferal biozones,
165 with an uncertainty of ±0.55 My for each stratigraphic interval (Bellanca et al., 1996;
166 Gambacorta et al., 2015). Lithology and published pyrite data (black triangles) are from
167 Gomes et al. (2016). Vertical purple line for $\Delta\delta^{34}S_{OS\text{-}py}$ shows $\delta^{34}S_{pyrite} = \delta^{34}S_{OS}$.

168

169 At Cismon, a narrow, ~35-cm-thick layer of TOC-rich (6.5 – 21.4 wt%) black shale
170 corresponds to part of the OAE-2 C-isotope excursion, although major portions of the C-
171 isotope excursion are absent due to hiatuses (Gambacorta et al., 2015; Gomes et al., 2016).
172 On either side of this lithologic unit, corresponding to the Bonarelli Layer, rocks from
173 Cismon are bedded layers of TOC-lean (≤ 0.05 wt%), micritic foraminiferal limestones
174 with occasional cherts and grey shales (Bellanca et al., 1996; Gambacorta et al., 2015).

Pyrite and carbonate-associated sulfate $\delta^{34}S$ values for a subset of the samples collected at outcrop in 2011 were previously published for a subset of mostly TOC-lean carbonates in the upper portion of the study interval (Gomes et al., 2016, Fig. 3). Here, we expand on that record and add OM $\delta^{34}S$ values where possible. Unfortunately, the limestones immediately surrounding the black shale unit are generally too TOC-lean and silicate-rich to permit spectroscopic analysis of S speciation or isotopic analysis of organic S by conventional EA-IRMS. For a point of comparison with OAE-2 shales, we analyzed a selection of limestones with 0.1–0.7 wt% TOC from lower in the section, representing approximately 96 – 100 Mya (spanning a 20-meter-thick zone from 37.5 m above the OAE-1a C-isotope excursion to 20 m below the onset of OAE-2, Fig. 3). In both the TOC-rich layer and earlier TOC-lean limestones, OM from Cismon is strongly ^{34}S-depleted, with $\delta^{34}S$ values averaging –37‰ during OAE-2 and –38.8‰ in the earlier samples. Pyrite is strongly ^{34}S-depleted in the deeper, moderately TOC-rich carbonates and somewhat less so in the black shale unit; pyrite $\delta^{34}S$ values for these lithologies average –49‰ and –42.7‰, respectively. The difference between the $\delta^{34}S$ values of pyrite and OM ($\Delta\delta^{34}S_{OS\text{-}py}$) averages 20.3‰ in the deeper carbonates but only 5.4‰ in the black shale.

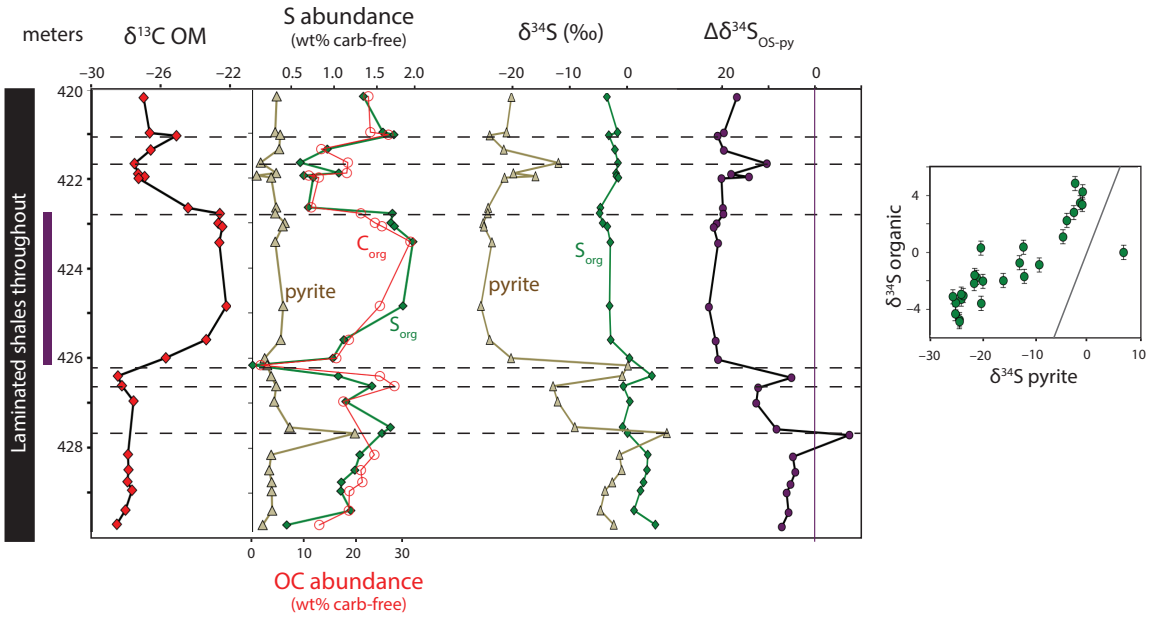

192

193 **Fig. 4 Demerara Rise record.** The purple bar at left represents the interpreted duration of
194 OAE-2 based on the C-isotope excursion. Dashed horizontal lines are intended as visual
195 aids to highlight patterns in the records. Vertical purple line for $\Delta\delta^{34}S_{OS\text{-}py}$ shows $\delta^{34}S_{pyrite}$
196 = $\delta^{34}S_{OS}$. Grey line in the right-hand panel shows a 1:1 line.

197

198 Sediments from Demerara Rise were deposited in the western tropical proto-North Atlantic
199 Ocean and were sampled as part of Ocean Drilling Program Leg 207 (Site 1258). Sediments
200 throughout the investigated section (with modified composite depths after Erbacher et al.,
201 2005) are generally described as laminated TOC-rich marl to black shales, with an apparent
202 average sedimentation rate of ~0.8 cm/kyr for the 4.0-m-thick C-isotope excursion (Owens
203 et al., 2016). On a carbonate-free basis, concentrations of TOC, organic S, and pyrite S
204 show no large-scale trends across the onset and termination of the OAE (Fig. 4; Owens et
205 al., 2016). Due to reduced carbonate concentrations during the C-isotope excursion, there
206 is a perceived increase in pyrite and TOC concentrations across this interval on a whole-

207 rock basis (Hetzel et al., 2009). Sediments are extremely OM-rich (Erbacher et al., 2005;
208 Hetzel et al., 2009), containing an average of 24 wt% TOC (Fig. 4; Owens et al., 2016) and
209 4.1 wt% organic S on a carbonate-free basis. These concentrations of organic S exceed
210 those of pyrite S by roughly five times. Organic matter $\delta^{34}S$ values are far less variable
211 than pyrite values; although samples after the onset of the OAE are slightly more ^{34}S-
212 depleted, all OM $\delta^{34}S$ values fall in a relatively narrow range between –4.9‰ and +4.8‰.
213 In contrast, pyrite $\delta^{34}S$ values decline substantially across the 2 meters of section prior to
214 the onset of OAE-2, from approximately –3‰ to–25‰, consistent with Hetzel et al. (2009).
215 Pyrite S-isotopes are relatively stable at these moderately ^{34}S-depleted compositions
216 throughout the OAE-2 C-isotope excursion and recover partly after the termination of the
217 event. Accordingly, $\Delta\delta^{34}S_{OS\text{-}py}$ at Demerara Rise increases from ~6‰ prior to OAE-2 to
218 ~21‰ during the OAE-2 C-isotope excursion, and the slope of the data in a pyrite–OM
219 $\delta^{34}S$ crossplot is much shallower than the 1:1 line. Like at Pont d'Issole, there are also
220 instances of locally ^{34}S-enriched pyrite in a sample without similar enrichment in organic
221 S (e.g., 427.7 m).
222

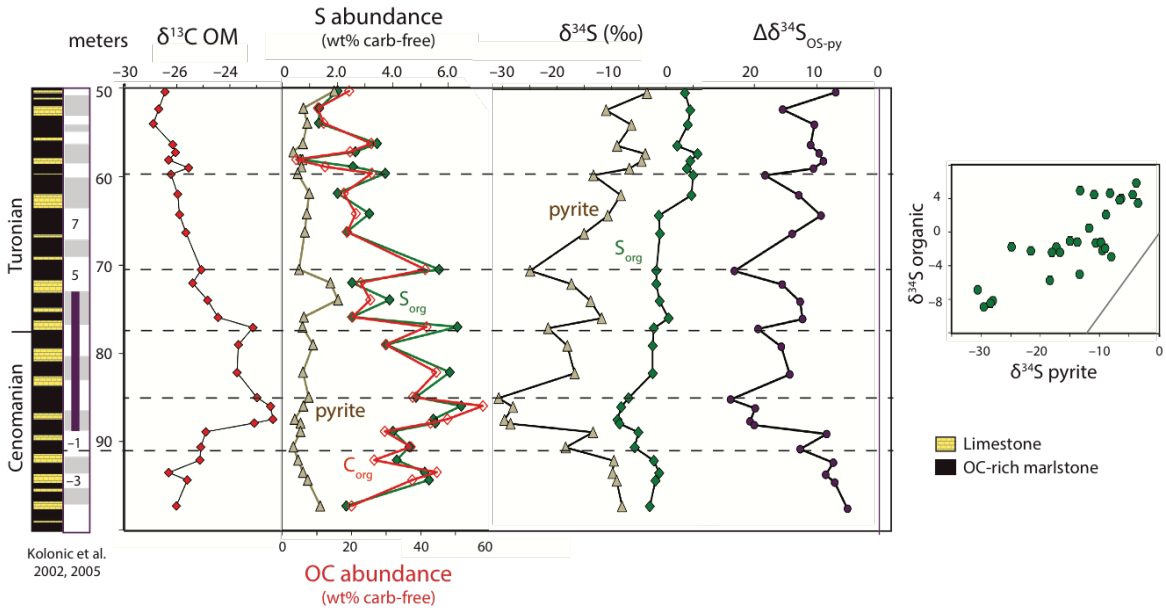

Fig. 5 Tarfaya Basin record. Lithology is shown at left, paired with recurrent sedimentary cycles from Kolonic (2002, 2005). Dashed horizontal lines indicate depths with relatively abundant OM and ^{34}S-depleted pyrite. The purple bar at left represents the interpreted duration of OAE-2 based on the C-isotope excursion. Vertical purple line for $\Delta\delta^{34}S_{OS\text{-}py}$ shows $\delta^{34}S_{pyrite} = \delta^{34}S_{OS}$. Grey line in the right-hand panel shows a 1:1 line.

Tarfaya Basin sediments (sampled from Shell exploration core S75) were deposited on the outer shelf of northwest Africa during a series of transgressive cycles associated with rifting of the southern North Atlantic Basin. High productivity and high sedimentation rates (averaging ~3.3 cm/kyr across the 16.5-meter-thick C-isotope excursion; Kolonic et al., 2005) supported the formation of extremely TOC-rich black shales and somewhat less TOC-rich carbonates, which alternate on apparently orbital timescales (Kolonic et al., 2005; 2002; Poulton et al., 2015; Fig. 5). This variation is also apparent in the $\delta^{34}S$ profile of pyrite, which is consistent with lower resolution data from Kolonic et al. (2002) and

Böttcher et al. (unpublished) as reported in Hetzel et al. (2009). Although we do not have the sampling density to resolve individual orbital cycles, TOC-rich layers generally contain relatively ^{34}S-depleted pyrite, as highlighted in dashed lines in Fig. 5. On top of this regular variation, the S-isotope profiles for TOC and pyrite have key similarities to those from Demerara Rise. TOC and pyrite δ^{34}S values prior to the onset of the OAE are between 0 and –10‰. By the onset of the OAE-2 C-isotope excursion, pyrite δ^{34}S values are at their minimum, generally –30‰. In the upper part of the core (depths < 65 m), post-OAE, pyrite δ^{34}S values return to pre-excursion values (–5 to –10‰). Organic matter δ^{34}S values express a muted drop from near –2‰ to a minimum of –8.9‰ at the onset of OAE-2 and a gradual increase thereafter, reaching ~4‰ in the top of the section.

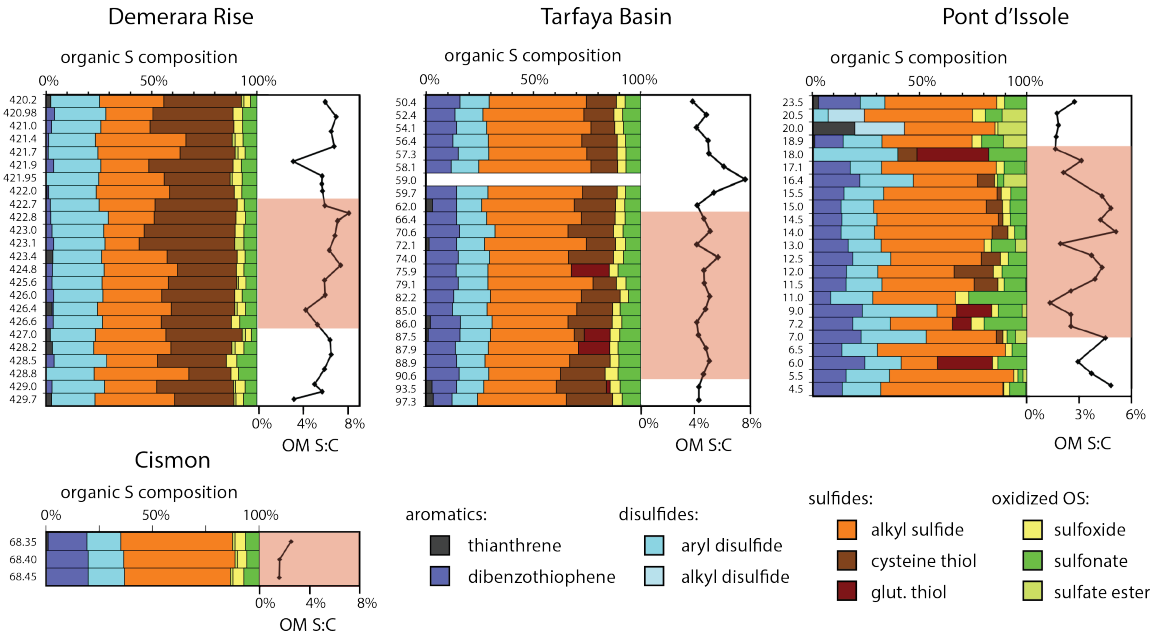

Fig. 6: Organic S speciation in organic matter. XAS and OM S:C (mol%) ratios show consistent organic S redox speciation among Demerara, Tarfaya, and Cismon samples and more variable speciation associated with local environmental change in Pont d'Issole. The

253 red shaded intervals correspond to the OAE-2 C-isotope excursion at each site. Categories
254 of reduced S structures (aromatic, disulfide, and sulfide) can be confidently distinguished,
255 but specific identifications within these groups (e.g., between sulfides and thiols) are
256 tentative.
257
258 X-ray absorption spectroscopy was used to quantify the relative contributions of different
259 forms of organic S to the total solvent- and acid-insoluble OM pool (Eglinton et al., 1994;
260 Vairavamurthy, 1998). At Demerara Rise and Tarfaya Basin, the speciation of organic S is
261 remarkably consistent before, during, and after the OAE-2 C-isotope excursion (Fig. 6),
262 contrasting the variation observed in the Pont d'Issole profile (Fig. 6; Raven et al., 2018).
263 Additionally, as summarized in Supplementary Table 1, the redox speciation of S-rich OM
264 (S:C $\geq$ 3%) is quite comparable at all four sites, with over half of organic S present as alkyl
265 sulfides and substantial amounts of disulfides and sulfonates. There are subtle, yet robust,
266 site-to-site differences in organic S speciation, with Demerara Rise OM richer in disulfides
267 and leaner in aromatic S forms than OM from Cismon, Tarfaya Basin, and Pont d'Issole
268 shales. In less strongly sulfurized samples from Pont d'Issole, the relative proportions of
269 oxidized organic S forms – sulfonates and sulfate esters – are generally higher at the
270 expense of alkyl sulfides (Raven et al., 2018).
271
272 **4. Discussion**
273
274 **4.1 Organic matter S:C ratios and local redox state**
275

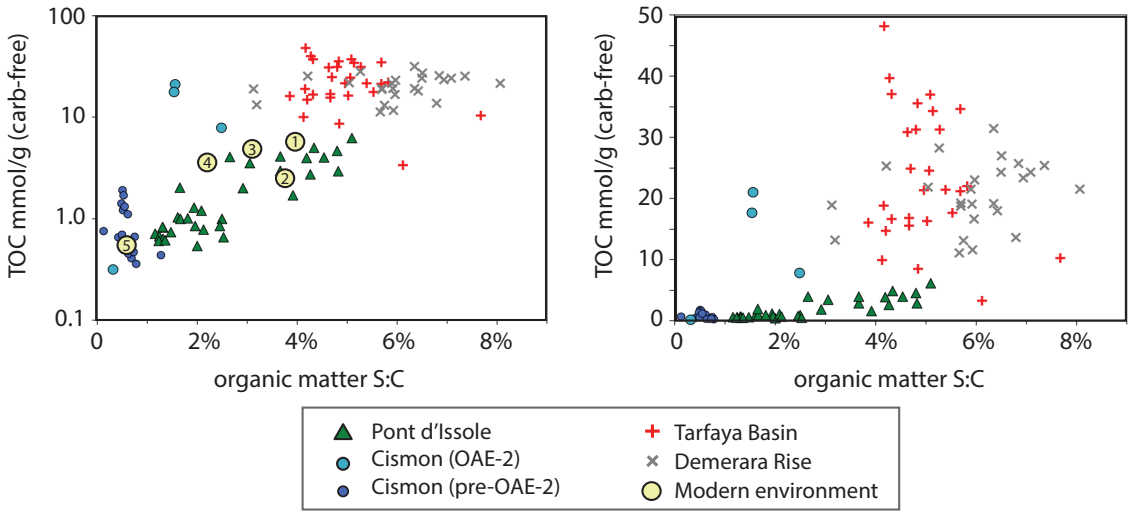

276

277 **Fig. 7 Global relationship between sulfurization intensity and TOC preservation.**
278 Relationships between the intensity of sulfurization (molar S:C ratio) and TOC
279 concentrations (mmol/g on a carbonate-free basis) are shown on log (left) and linear (right)
280 scales; for versions of these plots on a whole-rock basis, see Supplementary Figure 1.
281 Circled numbers on left panel refer to published values from modern environments: (1)
282 Cariaco Basin sediments (Werne et al., 2003); (2) the Peru Margin (Eglinton et al., 1994);
283 (3) the Namibian Margin (Dale et al., 2009); (4) Santa Barbara Basin sediments (Raven et
284 al., 2016b); and (5) Gulf of Lion sediments (this study; Supplementary Table 2).

285

286 The S:C ratio of OM provides an indicator of the relative intensity of sulfurization
287 reactions, with primary biomass values typically below 1 mol% and strongly sulfurized
288 OM exceeding ~3 mol% (Francois, 1987). OM S:C ratios can also be used to infer the
289 location of sulfurization (e.g., in particles sinking through the water column, at the
290 sediment-water interface, or within the sediments), which is largely a function of the redox
291 structure of the local depositional environment. Elevated OM S:C ratios require organic
292 substrates with a high density of functional groups available to react with (poly)sulfide; we

293 refer to these groups as functionally 'sulfurizable moieties,' recognizing that certain
294 moieties may be conditionally sulfurizable, contingent on the chemical and physical
295 properties of the environment (Blair and Aller, 2012). Still, we broadly expect the highest
296 concentrations of sulfurizable moieties in surface water, where fresh marine OM is
297 relatively rich in sulfurizable aldehydes, alcohols, and conjugated double bonds (Amrani
298 and Aizenshtat, 2004). The concentration of these moieties in particulate OM will decrease
299 with depth as microbial heterotrophs degrade and consume oxygen- and energy-rich
300 components of the milieu like sugars and proteins (Hedges et al., 1999).
301
302 Figure 7 illustrates how the relationship between the S:C ratio and concentration of TOC
303 for the four compiled OAE-2 sites compares with published data from modern
304 environments with different redox conditions. Bottom waters from Cariaco Basin (labeled
305 '1') are sulfidic below ~250 m water depth (Werne et al., 2003); bottom waters from the
306 Peru ('2') and Namibian ('3') Margins are O_2-depleted but rarely sulfidic, with sulfidic
307 sediments (Dale et al., 2009; Eglinton et al., 1994); bottom waters in Santa Barbara Basin
308 ('4') are intermittently oxic, with sulfidic sediments; and both the bottom water and
309 shallow sediments in the Gulf of Lion ('5') are oxic. Among these modern sites, S:C ratios
310 and OM concentrations are highest in sediments from the sulfidic Cariaco Basin and lowest
311 in sediments from the oxic Gulf of Lion. Of course, each of these sites is also affected by
312 unique chemical and physical characteristics of the environment. For example,
313 sedimentation rates are high on the Peru Margin due to the weathering of the Andes and
314 the abundance of detrital silica from diatoms, both of which presumably dilute OM
315 concentrations relative to other sites (Fig. 7). Despite this caveat, these modern sites

316 conform to a trend toward higher S:C ratios and higher OM concentrations associated with
317 increasingly O_2-limited environments.
318
319 The S:C ratios and TOC concentrations for modern sites overlap with the range of data
320 from Pont d'Issole and Cismon (Fig. 7). At least in terms of these bulk parameters, OM-
321 lean carbonate rocks from both sites resemble modern deposits from the oxic Gulf of Lion,
322 and more TOC-rich shales from Pont d'Issole resemble more O_2-limited sites like the Peru
323 Margin and Cariaco Basin. In a previous study that focused only on samples from Pont
324 d'Issole, positive correlations among OM S:C ratios, TOC concentrations, and OM $\delta^{34}S$
325 values were attributed to changes in local redox conditions (Raven et al., 2018), consistent
326 with these modern analogs. During more O_2-limited periods at Pont d'Issole, rapid OM
327 sulfurization reactions likely generated OM with S:C ratios near 5% in the water column
328 or near the sediment-water interface, where relatively fresh OM contains at least that
329 concentration of functionally sulfurizable moieties. During more oxic periods, gradual
330 sulfurization reactions in sediments affected older OM (≥10s of years) with a lower
331 concentration of sulfurizable moieties and generated OM with S:C ratios closer to 2%
332 (Raven et al., 2018).
333
334 Southern proto–North Atlantic OAE-2 samples extend the trend in Figure 7 toward even
335 greater OM concentrations and S:C ratios than those associated with bottom water anoxia
336 at Cismon, Pont d'Issole, and modern sites. We lack modern analogues for remarkable
337 hotspots of TOC burial like Tarfaya Basin, which had an outsized role in driving changes
338 in the OAE-2 C and S cycles (Kolonic et al., 2005; Sinninghe Damsté and Köster, 1998).

339 At both Demerara Rise and Tarfaya Basin, there is abundant evidence for water column
340 euxinia and at least intermittent photic zone anoxia. Finely laminated sediments from
341 Demerara Rise (Erbacher et al., 2005) contain only occasional benthic foraminifera
342 (Friedrich et al., 2006), iron speciation documents local sulfidic conditions (Owens et al.,
343 2016), and trace metals also suggest reducing local conditions (Hetzel et al., 2009) that
344 expand globally during the event (Owens et al., 2016). At Tarfaya, an anoxic and
345 commonly sulfidic water column is evidenced by iron speciation, organic petrography, and
346 the presence of biomarkers for phototrophic sulfide oxidizing bacteria (in nearby core S13;
347 Kuypers et al., 2002; Poulton et al., 2015). Still, there is also evidence for periodic, short-
348 lived intervals of less strongly reducing conditions (Poulton et al., 2015), potentially
349 contributing to slightly lower OM S:C ratios at this site than at Demerara. In general,
350 however, reducing conditions at both southern proto–North Atlantic sites could have
351 facilitated rapid, extensive sulfurization of a large pool of fresh OM in sinking particles
352 with a high concentration of functionally sulfurizable moieties (Sinninghe Damsté and
353 Köster, 1998). We emphasize that, in contrast with prior work, our conceptual model
354 invokes near–instantaneous reactions between OM with some concentration of sulfurizable
355 moieties and polysulfide, wherever sulfide and oxidants are first available in the
356 environment. Polysulfide 'availability' for sulfurization will depend on microbial sulfate
357 reduction rates, oxidant availability, and competition with Fe; importantly, however, it does
358 not necessarily imply measurable free sulfide in the ('bulk') water column.
359
360 We can also compare OM from Demerara Rise and Tarfaya Basin with the results of
361 laboratory sulfurization experiments utilizing fresh algal biomass or model compounds. In

362 the presence of excess polysulfides, lipids and carbohydrates sulfurize to form
363 macromolecular material in which characteristic components have S:C ratios around 2–3%
364 (Gelin et al., 1998) and ~6.7% (van Dongen et al., 2003), respectively. For dissolved
365 organic matter, bulk molar S:C ratios can apparently be much higher, reaching as much as
366 15% in recent experiments (Pohlabeln et al., 2017). Still, the average S:C ratios of (bulk,
367 particulate) OM from Tarfaya Basin (5.0%), Demerara Rise (5.9%), and Cismon shales
368 (5.0%) indicate that the OM sulfurizing in these environments had a concentration of
369 sulfurizable moieties similar to the constituents of fresh, carbohydrate–rich algal biomass.
370 Experimental data thus lend credence to the hypothesis that rapid, likely particle-hosted,
371 sulfurization drove OM preservation in the water columns of both Tarfaya Basin and
372 Demerara Rise.
373
374 Broadly speaking, the relationship between S:C ratio, OM preservation, and local redox
375 structure appears to be generalizable for marine environments, with the highest S:C ratios
376 and TOC concentrations supported by rapid, particle-hosted sulfurization under strongly
377 O_2-limited conditions. The observation that OM sulfurization is an apparently major
378 control on OM burial in diverse redox settings invites parameterization and application of
379 this trend to models of carbon cycling on local to global scales and throughout the geologic
380 record.
381
382
383 **4.2 Interpreting organic matter and pyrite $\delta^{34}S$ records**
384

385 To first order, the sulfur isotope compositions of pyrite and organic S reflect the $\delta^{34}S$ value
386 of sulfide and/or polysulfide in the environment where that solid phase formed, with OM
387 commonly ~5–10‰ more ^{34}S-enriched than coexisting pyrite (Anderson and Pratt, 1995).
388 Accordingly, S–isotope ratios – of both pyrite and sulfurized OM – provide potentially
389 powerful archives of information about the availability and distribution of sulfide in the
390 environment. Several primary factors affect the integrated (poly)sulfide $\delta^{34}S$ value
391 recorded in pyrite and OM, including (1) the $\delta^{34}S$ value of the sulfate used in microbial
392 sulfate reduction (MSR, Fike and Grotzinger, 2008); (2) the fractionation factor associated
393 with MSR (ε_{MSR}, Kaplan and Rittenberg, 1964); (3) the position of the chemocline relative
394 to diffusively 'closed' sediments (Jorgensen, 1979) and (4) the concentration of sulfate and
395 resulting depth of sulfate depletion (Adams et al., 2010). Importantly, all of these processes
396 impact the distribution and/or $\delta^{34}S$ value of (poly)sulfide in the environment and should
397 therefore impact the S-isotope composition of both pyrite and OM, generating roughly
398 parallel $\delta^{34}S$ profiles. If pyrite and OM $\delta^{34}S$ profiles are not parallel, then we need to invoke
399 processes that affect these sinks differently.
400

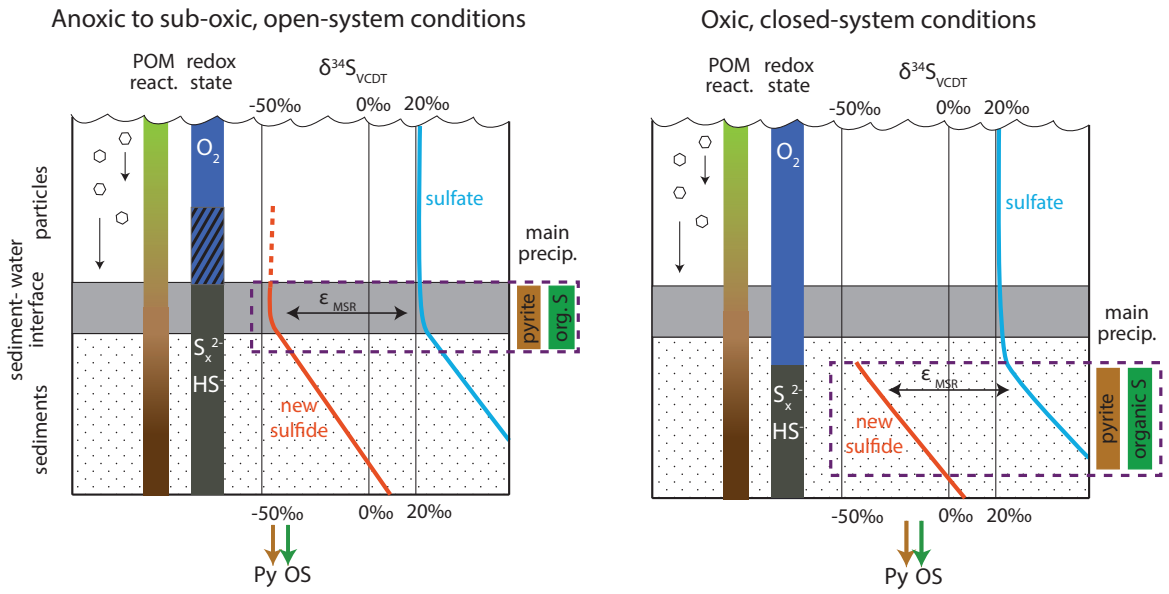

Fig. 8: Model for organic S and pyrite formation at Pont d'Issole and Cismon. The color scale labeled "POM react." represents a generalized decline in the reactivity of particulate OM with age since export from the photic zone. At left, the dashed red line and hatched redox state depict differences between sub-oxic and anoxic conditions. Under anoxic conditions, the zone of precipitation for pyrite and organic S would move upward with the chemocline. Diagram is not to scale.

At Pont d'Issole, OM and pyrite $\delta^{34}S$ profiles move in roughly parallel between the TOC-rich and TOC-lean layers associated with OAE-2 (Fig. 2). Accordingly, these phases appear to be primarily recording changes in the $\delta^{34}S$ value or distribution of sulfide in the environment. Like OM $\delta^{34}S$ values at this site (Raven et al., 2018), pyrite $\delta^{34}S$ values describe the extent to which sulfate was diffusively limited in sediments, shown schematically in Fig. 8. Under conditions where O_2 concentrations are drawn down to zero at roughly the sediment-water interface (which we call 'sub-oxic' in Fig. 8), MSR in the shallowest sediments can access the open-ocean pool of seawater sulfate with an

417 unfractionated $\delta^{34}S$ value, and the resulting strongly ^{34}S-depleted sulfide from MSR is
418 recorded in both pyrite and OM. Under more 'oxic' conditions, O_2 penetrates deeper in the
419 sediments and microbial sulfate reduction occurs in a diffusively sulfate–limited
420 environment. As available sulfate is consumed with some fractionation (ε_{MSR}), residual
421 sulfate in porewater becomes enriched in ^{34}S, and the organic and inorganic sulfur pools
422 that precipitate within such a (partially) closed system have higher integrated $\delta^{34}S$ values
423 than those formed in open systems. At Pont d'Issole, S–isotope evidence for more closed-
424 system MSR is also associated with smaller amounts of preserved OM with a lower S:C
425 ratio (Raven et al., 2018).
426
427 Both organic S and pyrite from Cismon black shales are strongly ^{34}S-depleted, consistent
428 with generally open-system pyrite and organic S formation during the OAE C-isotope
429 excursion. These low $\delta^{34}S$ values resemble S-isotope values observed in sediments from
430 modern sulfidic basins, which have been attributed to open-system pyritization (Lyons et
431 al., 2003). As noted by the dashed vertical red line in Fig. 8, the critical sulfidic
432 environment(s) hosting these reactions could be very shallow sediments and/or particles
433 sinking through the water column. In deeper carbonates from Cismon, OM is only weakly
434 sulfurized (S:C averaging 0.6 mol%), so the connection between dissolved (poly)sulfides
435 and the $\delta^{34}S$ value of OM is less robust. High $\Delta\delta^{34}S_{OS\text{-}pyrite}$ values for samples with low S:C
436 ratios (≤1.0 mol%) could reflect contributions from detrital, biomass, or macrofaunal
437 exudate sources to organic S in addition to sulfurization.
438

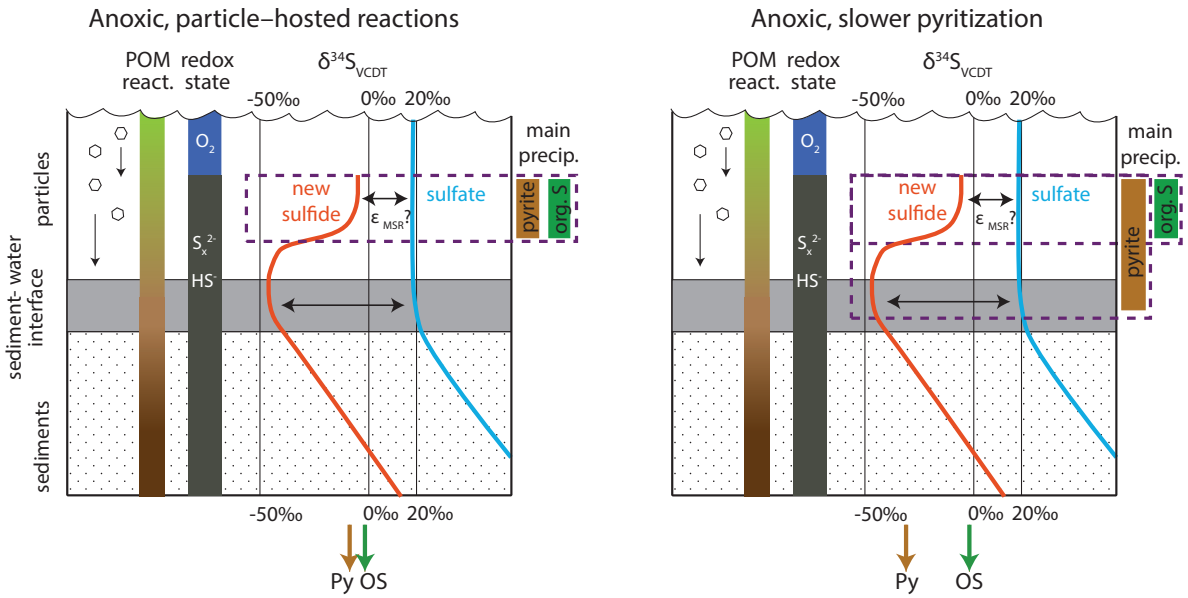

439

440 **Fig. 9 Proposed model for OAE-2 $\delta^{34}S$ records at Tarfaya and Demerara.** Left panel
441 shows hypothesized conditions ≥190,000 yrs before the onset of OAE-2. Right panel shows
442 a scenario for explaining pyrite and OM $\delta^{34}S$ values during the early part of the OAE-2 C-
443 isotope excursion. Changes in available Fe could slow the rate of pyrite formation relative
444 to OM sulfurization and generate more ^{34}S-depleted pyrite without impacting the S-isotope
445 composition of OM. The color scale labeled "POM react." represents a generalized decline
446 in the reactivity of particulate OM with age since export from the photic zone. Diagram is
447 not to scale.

448

449 Different processes impact $\delta^{34}S$ patterns at Tarfaya Basin and Demerara Rise. A wealth of
450 data supports the idea that the Tarfaya Basin and Demerara Rise water columns were
451 typically euxinic before and after OAE-2, which would imply open-system S cycling that
452 leads to ^{34}S-depleted pyrite and OM (Hetzel et al., 2009; Poulton et al., 2015). Yet, $\delta^{34}S$
453 values of pyrite and OM from both of these sites are near –5‰ at these times, much more
454 ^{34}S-enriched than samples from other sites with open-system MSR. To reconcile these

455 observations, we propose that the $\delta^{34}S$ values recorded in plentiful OM at Tarfaya Basin
456 and Demerara Rise do reflect the S-isotope composition of sulfide in sinking particles, and
457 that this sulfide was relatively ^{34}S-enriched (Fig. 9; below). Similarly, there is limited
458 evidence for the existence of transiently ^{34}S-enriched sulfide in particles from Cariaco
459 Basin during a period of peak productivity and sinking OM flux (Raven et al., 2016a).
460 Particles from this period contain abundant C_{20} thiophene, a common sulfurized
461 organosulfur compound, with a much more ^{34}S-enriched composition (–14.1 to 3.1‰) than
462 during other times (–29.9 to –18.2‰), indicating at least the transient existence of
463 relatively ^{34}S-enriched (poly)sulfide in particles (Raven et al., 2016a) despite deep basin
464 sulfide $\delta^{34}S$ values near –30‰ (Li et al., 2010). The dramatic increase in inferred sulfide
465 $\delta^{34}S$ values in particles from Cariaco Basin, Tarfaya Basin, and Demerara Rise (Fig. 9)
466 contrasts with the slight (~5‰) increases in sulfide $\delta^{34}S$ value frequently observed in the
467 uppermost portion of modern sulfidic water columns (Lyons et al., 2003), which are
468 attributed to oxidative S-cycling microorganisms and/or abiotic sulfide oxidation. Thus,
469 the $\delta^{34}S$ values of strongly sulfurized OM and pyrite in TOC-rich sediments may capture
470 the signature of MSR occurring rapidly in sinking particles.
471
472 The large fluxes of fresh OM that reached O_2-limited parts of the environment in both
473 Tarfaya Basin and Demerara Rise make these sites likely candidates for the operation of
474 rapid, substrate-replete MSR, which could lead to relatively ^{34}S-enriched sulfide in
475 particles via smaller isotope fractionations during sulfate reduction, sulfate drawdown
476 within diffusively limited microenvironments, or both. The fractionation factor associated
477 with MSR (ε_{MSR}) is highly variable and depends broadly on MSR rate (Kaplan and

478 Rittenberg, 1964). Although most marine systems have apparent S-isotope fractionation
479 factors closer to the equilibrium fractionation between sulfate and sulfide of 72‰, low ε_{MSR}
480 values (<25‰) are associated with high rates of cell-specific MSR, on the order of >25
481 fmol H_2S/cell/day (Wenk et al., 2017), observed for sulfate reducers in laboratory settings
482 with plentiful carbon substrates and nutrients. These "small" S-isotope fractionations are
483 consistent with the 20–30‰ difference between seawater sulfate (at ~19‰) and apparent
484 particle-hosted sulfide observed at Tarfaya Basin and Demerara Rise. Alternatively or in
485 addition to changes in ε_{MSR}, if particles are sufficiently large (>> 1 mm), it is possible for
486 sulfate to become diffusively limited within particle microenvironments (Louca and
487 Crowe, 2017), especially given relatively low seawater sulfate concentrations at this time
488 (Lowenstein et al., 2003; Owens et al., 2013; Gomes et al., 2016). Very high rates of MSR
489 could therefore drive the remaining sulfate pool within microenvironments toward higher
490 $\delta^{34}S$ values and contribute to relatively ^{34}S-enriched sulfide.
491
492 The alternative explanation for our results attributes the relatively ^{34}S-enriched
493 composition of pyrite and OM at Tarfaya Basin and Demerara Rise prior to the onset of
494 the OAE to their formation from sediment porewater. Importantly, it also requires that these
495 phases form semi-continuously during burial to the depths at which sulfate is nearly fully
496 drawn down, to integrate to bulk compositions near –5‰. Barring extreme sedimentation
497 events, this implies maximum OM sulfurization rates on the timescales of at least tens to
498 hundreds of years – sufficient to accumulate a diffusively limiting layer – not the days to
499 weeks observed in Cariaco particles and laboratory experiments. Additionally, this
500 explanation for Tarfaya Basin and Demerara Rise $\delta^{34}S$ patterns is difficult to reconcile with

501 the S:C ratio of OM. For OM to incorporate up to 6 mol% S gradually over at least years
502 of aging, that OM must have retained a high density of sulfurizable moieties that were
503 somehow also effectively inaccessible to heterotrophs. Theoretically, this could result from
504 enhanced preservation mechanisms other than sulfurization, notably physical protection by
505 association with clays or other mineral surfaces (Hedges and Keil, 1995) or the absence of
506 bioturbating macrofauna (Middelburg and Levin, 2009). Still, the sheer abundance of OM
507 in Tarfaya Basin and Demerara Rise sediments would overwhelm available clays, and it is
508 difficult to envision a mechanism to sulfurize OM after many years of effective physical
509 protection. We therefore consider a purely closed-system sedimentary origin for the
510 moderately ^{34}S-enriched OM at Tarfaya Basin and Demerara Rise improbable.
511
512 Similar to OM throughout the section, pyrite in the lowest part of the section at both
513 Tarfaya Basin and Demerara Rise has relatively high $\delta^{34}S$ values. Under these pre-OAE-2
514 conditions, the offset between pyrite and OM $\delta^{34}S$ values is 5–10‰, similar to the offset
515 observed in other environments that are thought to host open-system concurrent
516 pyritization and OM sulfurization (Cariaco Basin, Cismon). Starting significantly before
517 the onset of OAE-2, pyrite $\delta^{34}S$ begins to move independently of OM $\delta^{34}S$, increasing
518 $\Delta\delta^{34}S_{OS\text{-}py}$ values. Little-to-no concurrent shift is seen in the OM $\delta^{34}S$ record. Similarly,
519 XAS data show a lack of change in the speciation of organic S across the onset of OAE-2
520 at both Tarfaya Basin and Demerara Rise (Fig. 5), suggesting consistent conditions for OM
521 sulfurization throughout. Therefore, the shift in pyrite $\delta^{34}S$ values is caused by a process
522 that impacts the kinetics of one sulfide sink relative to the other, not by a change in sulfide
523 distribution or ε_{MSR} in the environment. In the case of pyrite at the onset of OAE-2 at

524 Tarfaya and Demerara Rise, the observed shift indicates that the zone of pyrite formation
525 expanded into deeper portions of the water column and/or sediment, integrating more ^{34}S-
526 depleted sulfide generated from MSR at more typical (slow) environmental rates (Fig. 9)
527 for reasons we discuss below.
528
529 **4.3 Global pyrite δ^{34}S patterns and OAE-2 implications**
530

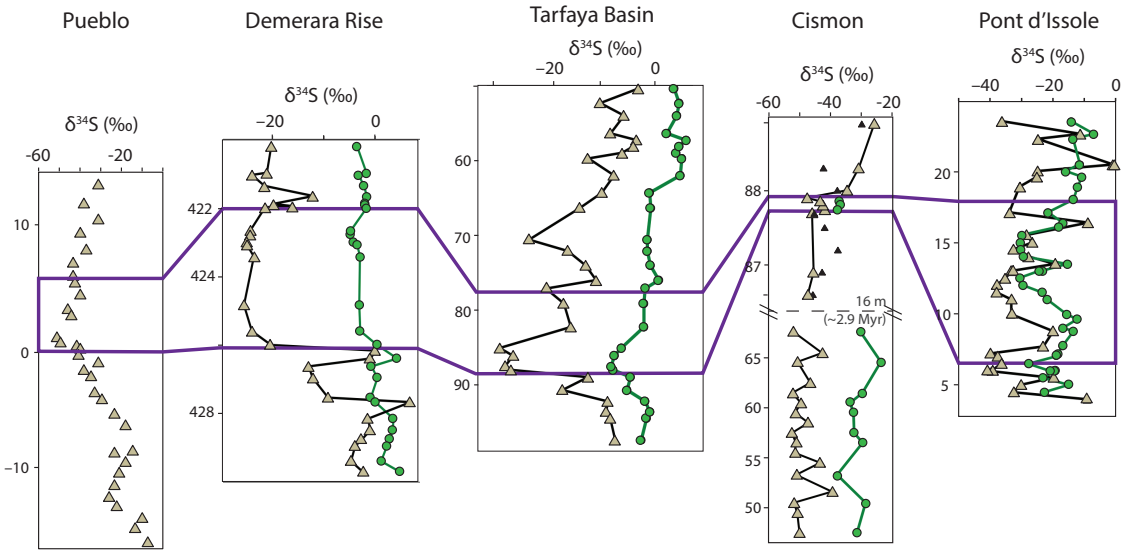

531
532 **Fig. 10 Summary of δ^{34}S records across OAE-2.** Green circles show OM δ^{34}S values and
533 brown triangles show pyrite δ^{34}S values. Pueblo data are from Adams et al. (2010). The
534 gap in the Cismon y-axis represents 16 m of TOC-lean carbonates (~2.9 Myr), and small
535 black triangles are previously published pyrite (CRS) data (Gomes et al., 2016). The C-
536 isotope excursion, representing an estimated 500 kyr of accumulation, is outlined in purple.
537 Pyrites from Demerara Rise, Tarfaya Basin, and Pueblo all become more ^{34}S-depleted
538 leading up to the onset of OAE-2.
539

The decrease in pyrite $\delta^{34}S$ values prior to the onset of OAE-2 appears to be a widespread phenomenon, with remarkably similar profiles from Demerara Rise, Tarfaya Basin, and the Western Interior Seaway (Pueblo; Adams et al., 2010). Because the ~20‰ negative $\delta^{34}S$ shift in pyrite at Tarfaya and Demerara is not observed in the $\delta^{34}S$ profile of OM, it is not likely to primarily reflect changes in the spatial distribution or $\delta^{34}S$ of dissolved sulfide in the environment. Instead, we propose that pyrite $\delta^{34}S$ patterns record changes in marine iron supply across OAE-2, which impacted the kinetics of pyrite precipitation and extended the zone of pyrite precipitation deeper in the sedimentary profile.

The highly reactive iron available for pyritization in marine environments is sourced from a mixture of detrital iron from the continents, hydrothermal iron from spreading ridges, and remobilized iron from biogeochemical cycling in shelf sediments (Poulton and Raiswell, 2002). Most sediments from the southern proto–North Atlantic during OAE-2 have elevated Fe_T/Al ratios (>0.5, the crustal average value) and near–zero $\delta^{56}Fe$ compositions, suggesting that a significant component of the iron delivered to these sites was from hydrothermal sources (Owens et al., 2012). The processes that facilitate the transport of hydrothermally sourced iron remain subjects of active research, but appear to involve stabilization of Fe^{3+} in colloidal or nanoparticulate phases (Fitzsimmons et al., 2017). Hydrothermal iron that encounters dissolved sulfide can precipitate as an Fe-sulfide and be trapped in place as pyrite, restricting the amount of iron that can be transported through euxinic basins to distal sites. In contrast, iron is highly mobile in anoxic but non-sulfidic seawater. The delivery of iron to Demerara Rise and Tarfaya Basin was therefore likely

562 sensitive to the redox state of nearby environments, and hydrothermal iron delivery could
563 have been significantly curtailed by nearby euxinia.
564
565 In addition to impacting the total flux of iron transported throughout the basin, expanding
566 anoxia is likely to affect its mineralogy. The source of Fe for pyritization is commonly
567 presumed to be dissolved Fe^{2+}, which can be released from Fe^{III}-bearing minerals by
568 reduction either abiotically with bisulfide (Canfield, 1989) or biotically by Fe-reducing
569 microorganisms. The rates of both types of iron reduction vary depending on the
570 mineralogy and specific surface area of the Fe^{III} involved: poorly crystalline oxyhydroxides
571 like ferrihydrite and lepidocrocite are reduced within hours to days, while crystalline oxides
572 and oxyhydroxides like goethite and hematite are reduced more slowly, and Fe-bearing
573 silicates can persist for millennia (Poulton and Canfield, 2005; Raiswell and Canfield,
574 1996). Where concentrations of Fe^{2+} and sulfide in solution are sufficiently high, pyrite
575 precipitation is generally thought to proceed via precipitation of an iron monosulfide
576 intermediate that subsequently converts to pyrite. Intriguingly, Wan et al. (2017) recently
577 described a second category of pyritization mechanism with the potential to drive pyrite
578 formation where Fe^{III}–oxide surfaces are plentiful and vastly exceed the available HS^-.
579 Under these conditions, ferric hydroxide surfaces can mediate the rapid nucleation of pyrite
580 via the formation of $>Fe^{II}S_2^-$, making redox interfaces and sinking particles with high
581 Fe^{III}:HS^- ratios potential hotspots for surface-mediated pyritization of ferric hydroxides.
582 Expanding regional euxinia would likely reduce the transport of ferric hydroxides to
583 euxinic sites like Demerara Rise and Tarfaya Basin, lowering the Fe^{III}:HS^- ratio near
584 critical interfaces in the water column. The resulting change in the relative importance of

585 surface-mediated versus dissolved-phase pyritization mechanisms could thus contribute to
586 the observed shift in pyrite $\delta^{34}S$. Regardless of the significance of this particular
587 mechanism, changing regional redox could impact the mineralogy of remobilized Fe more
588 broadly by changing the rates and/or environmental conditions of (oxy)hydroxide
589 formation during repetitive redox cycling, generating a different suite of Fe^{III} minerals that
590 re-release Fe^{2+} into the depositional environment at diverse rates. The bulk pyrite $\delta^{34}S$
591 records we present here reflect the integrated pool of pyrite derived from precipitation on
592 multiple timescales following Fe^{III}–mineral (re-)reduction as well as potentially from ferric
593 hydroxide surface–mediated reactions. Separating these various contributors to bulk pyrite
594 records will be essential for understanding how expanding regional anoxia and euxinia
595 impacted the abundance and mineralogy of iron sources and, by extension, the kinetics of
596 pyritization.
597
598 Trace metal concentrations and thallium isotopes from Demerara Rise provide evidence
599 for the expansion of regional to more global anoxia prior to the onset of the OAE-2 C-
600 isotope excursion (Ostrander et al., 2017; Owens et al., 2016). Like iron, the redox-
601 sensitive elements Zn, V, and Mo are readily sequestered in anoxic and/or sulfidic
602 sediments, and this process is thought to be responsible for their apparent removal from
603 seawater prior to OAE-2 (Owens et al., 2016). Using an extrapolation of the estimated
604 OAE-2 linear sedimentation rate (0.8 cm/kyr) to 427.5 m, pyrite $\delta^{34}S$ values at Demerara
605 begin to decrease ~190 kyr before the onset of OAE-2. This depth corresponds to the initial
606 drop in concentrations of Zn in this core, a sensitive indicator of anoxia with a short
607 residence time (~11 kyr, Little et al., 2014) that implies a global increase in non-sulfidic,

608 anoxic conditions significantly before the onset of OAE-2. The decrease in pyrite $\delta^{34}S$
609 values is complete by the onset of the OAE, in sediments evidencing drawdown of even
610 sulfide-sensitive Mo, indicating prevalent sulfidic environments (Owens et al., 2016). The
611 gradual pre-OAE pyrite $\delta^{34}S$ shift at Demerara thus corresponds to a period of
612 intensification of regional to global anoxia prior to the OAE and an expansion of sulfidic
613 conditions globally (Owens et al., 2013).
614
615 Changes in the delivery of iron to sites in the southern proto–North Atlantic could have
616 generated the shift in pyrite $\delta^{34}S$ that we observe by slowing the kinetics of pyrite
617 formation. For example, if the combination of expanding euxinia and volcanic activity
618 caused the main source of Fe at these sites to switch from more hydrothermally sourced,
619 organic–complexed Fe^{III} to detrital or volcanic crystalline oxy-hydroxides, the rate of Fe^{2+}
620 release to solution in sinking marine particles could have dropped dramatically. The
621 conceptual model put forth in Fig. 9 predicts that this scenario would yield more ^{34}S-
622 depleted pyrite overall. Importantly, this could occur while the total quantity of pyrite
623 eventually buried remained nearly constant.
624
625 At Pueblo and Tarfaya Basin, the onset of the shift toward more ^{34}S-depleted pyrite is
626 staggered relative to Demerara Rise (Fig. 10). Using published interpolated Ar-Ar ages
627 from ammonite biozones, pyrite $\delta^{34}S$ values at Pueblo drop in two stages at ~400 kyr and
628 ~200 kyr before the onset of OAE-2 (Adams et al., 2010). At Tarfaya Basin, if we
629 extrapolate estimated OAE-2 accumulation rates (3.3 cm/kyr) similar to Demerara, then
630 the pyrite $\delta^{34}S$ shift occurs ~82 kyr before the OAE. Osmium, strontium, and other

631 geochemical proxies indicate regional heterogeneity in hydrothermal activity in different
632 ocean basins at this time (du Vivier et al., 2014), which would also impact hydrothermal
633 iron fluxes (Owens et al., 2012). Importantly, the Western Interior Seaway has a different
634 redox structure leading up to OAE-2 than the rest of the proto-North Atlantic and Tethys,
635 which likely leads to differences in the history of iron cycling among these sites.
636
637 Records from OAE-2 exemplify how the timing and location of pyritization can be affected
638 by changes in iron supply in addition to changes in sulfur cycling. They also suggest that
639 organic S should be incorporated into future models for the S cycle for OAEs. For example,
640 because organic S is more typically more ^{34}S-enriched than pyrite, previous estimates for
641 the extent of euxinia during OAE-2 based on S-isotope mass balance (e.g., Owens et al.,
642 2013) may be conservative. OM sulfurization could have been an important factor for
643 driving high organic carbon mass accumulation rates even for localities with low TOC
644 (Owens et al., 2018), supporting massive global OM burial. By investigating the S-isotope
645 behavior of both pyrite and OM, we can begin to take full advantage of these complex and
646 powerful archives.
647
648 **5. Conclusions**
649 Rapid, particle-hosted OM sulfurization may have been a central process facilitating
650 enhanced OM preservation across large swaths of the Tethys and North Atlantic Oceans
651 before, during, and after OAE-2. Explicit consideration of rapid OM sulfurization in O_2-
652 limited environments thus has the potential to improve models of TOC preservation and
653 remineralization in both modern and ancient systems.

654

655 Paired OM and pyrite $\delta^{34}S$ profiles make it possible to disentangle the effects of chemocline
656 position, sulfate reduction rate, and regional-to-global geochemical perturbations on S-
657 isotopes in the rock record. In the several hundred thousand years leading up to the onset
658 of OAE-2, pyrite and OM $\delta^{34}S$ records indicate a globally widespread change in the timing
659 of pyrite formation relative to OM sulfurization, which both S-isotope and speciation
660 (XAS) data argue occurred consistently across this interval. A regional expansion of
661 euxinic conditions and changes in volcanic activity may have contributed to changes in the
662 speciation of iron available for pyritization and thus to the relatively slow formation of
663 relatively ^{34}S-depleted pyrite during the OAE. This change in global iron cycling could not
664 be identified from pyrite $\delta^{34}S$ profiles alone, underscoring the value and untapped potential
665 of paired pyrite – OM S-isotope records for exploring the geologic record.

666

667

668 **Acknowledgements**

669 We are grateful for financial support to M.R.R. from the Agouron Institute (Geobiology
670 Post-doctoral Fellowship) and to Itay Halevy (Weizmann Institute, Israel), Matt Hurtgen,
671 and Brad Sageman (Northwestern University, USA) for valuable discussions. Melanie
672 Suess, Jen Houghton, and Stephanie Moore provided technical support for analyses at
673 Washington University in St. Louis. Tarfaya and Demerara samples were obtained via
674 Wolfgang Kuhnt (Kiel University) and IODP, respectively. Virgil Pasquier (Weizmann
675 Institute, Israel) provided Gulf of Lion samples. JDO would like to acknowledge support
676 from NASA Exobiology (80NSSC18K1532). This work was enhanced by XAS analyses

677 at the Stanford Synchrotron Radiation Laboratory under User Proposal 4885, as well as by
678 the efforts of SSRL staff. Use of the Stanford Synchrotron Radiation Lightsource, SLAC
679 National Accelerator Laboratory, is supported by the U.S. Department of Energy, Office
680 of Science, Office of Basic Energy Sciences under Contract No. DE-AC02-76SF00515.

681

682 **Supplemental Information:**

683 Fig. S1: whole-rock basis version of Fig. 6

684 Table S1: Average relative abundances of organic S moieties for sections spanning OAE-
685 2 by XAS

686 Table S2: Gulf of Lion average composition

687 Table S3: Compiled geochemical results

688 Table S4: Compiled XAS results

689

690 **References**

691 Adams, D.D., Hurtgen, M.T., Sageman, B.B., 2010. Volcanic triggering of a
692 biogeochemical cascade during Oceanic Anoxic Event 2. Nature Geoscience 3, 201–
693 204.

694 Amrani, A., Aizenshtat, Z., 2004. Mechanisms of sulfur introduction chemically
695 controlled: δ34S imprint. Organic Geochemistry 35, 1319–1336.
696 doi:10.1016/j.orggeochem.2004.06.019

697 Anderson, T.F., Pratt, L.M., 1995. Isotopic evidence for the origin of organic sulfur and
698 elemental sulfur in marine sediments. In: Geochemical Transformations of
699 Sedimentary Sulfur. ACS Symposium Series, vol. 612, 378–396. American Chemical
700 Society, Washington DC.

701 Bellanca, A., Claps, M., Erba, E., Masetti, D., Neri, R., 1996. Orbitally induced
702 limestone/marlstone rhythms in the Albian—Cenomanian Cismon section (Venetian
703 region, northern Italy): Sedimentology, calcareous and siliceous plankton
704 distribution, elemental and isotope geochemistry. Palaeogeography 126, 227–260.
705 doi:10.1016/S0031-0182(96)00041-7

706 Blair, N.E., Aller, R.C., 2012. The Fate of Terrestrial Organic Carbon in the Marine
707 Environment. Annu. Rev. Mar. Sci. 4, 401–423.

708 Boussafir, M., Gelin, F., Lallier-Verges, E., Derenne, S., Bertrand, P., Largeau, C., 1995.
709 Electron microscopy and pyrolysis of kerogens from the Kimmeridge Clay
710 Formation, UK: Source organisms, preservation processes, and origin of microcycles.
711 Geochimica et Cosmochimica Acta 59, 3731–3747.

712 Canfield, D.E., 1989. Reactive iron in marine sediments. Geochimica et Cosmochimica
713 Acta 53, 619–632. doi:10.1016/0016-7037(89)90005-7

714 Canfield, D.E., Raiswell, R., Westrich, J.T., Reaves, C.M., 1986. The use of chromium
715 reduction in the analysis of reduced inorganic sulfur in sediments and shales.
716 Chemical Geology 54, 149–155.

717 Dale, A.W., Bruchert, V., Alperin, M., Regnier, P., 2009. An integrated sulfur isotope
718 model for Namibian shelf sediments. Geochimica et Cosmochimica Acta 73, 1924–
719 1944. doi:10.1016/j.gca.2008.12.015

720 du Vivier, A.D.C., Selby, D., Sageman, B.B., Jarvis, I., Gröcke, D.R., Voigt, S., 2014.
721 Marine 187Os/188Os isotope stratigraphy reveals the interaction of volcanism and
722 ocean circulation during Oceanic Anoxic Event 2. Earth and Planetary Science
723 Letters 389, 23–33. doi:10.1016/j.epsl.2013.12.024

724 Eglinton, T.I., Irvine, J.E., Vairavamurthy, A., Zhou, W., Manowitz, B., 1994. Formation
725 and diagenesis of macromolecular organic sulfur in Peru margin sediments. Organic
726 Geochemistry 22, 781–799. doi:10.1016/0146-6380(94)90139-2

727 Erbacher, J., Friedrich, O., Wilson, P.A., Birch, H., Mutterlose, J., 2005. Stable organic
728 carbon isotope stratigraphy across Oceanic Anoxic Event 2 of Demerara Rise,
729 western tropical Atlantic. Geochemistry Geophysics Geosystems 6, 714–9.
730 doi:10.1029/2004GC000850

731 Fike, D.A., Grotzinger, J.P., 2008. A paired sulfate–pyrite δ34S approach to
732 understanding the evolution of the Ediacaran–Cambrian sulfur cycle. Geochimica et
733 Cosmochimica Acta 72, 2636–2648. doi:10.1016/j.gca.2008.03.021

734 Fitzsimmons, J.N., John, S.G., Marsay, C.M., Hoffman, C.L., Nicholas, S.L., Toner,
735 B.M., German, C.R., Sherrell, R.M., 2017. Iron persistence in a distal hydrothermal
736 plume supported by dissolved–particulate exchange. Nature Geosci 10, 195–201.
737 doi:10.1038/ngeo2900

738 Francois, R. (1987). A study of sulphur enrichment in the humic fraction of marine
739 sediments during early diagenesis. Geochimica Et Cosmochimica Acta, 51, 17–27.

740 Friedrich, O., Erbacher, J., Wilson, P. A., Moriya, K., & Mutterlose, J. (2009).
741 Paleoenvironmental changes across the Mid Cenomanian Event in the tropical
742 Atlantic Ocean (Demerara Rise, ODP Leg 207) inferred from benthic foraminiferal
743 assemblages. Marine Micropaleontology, 71(1-2), 28–40.
744 http://doi.org/10.1016/j.marmicro.2009.01.002

745 Gambacorta, G., Jenkyns, H.C., Russo, F., Tsikos, H., Wilson, P.A., Faucher, G., Erba,
746 E., 2015. Carbon- and oxygen-isotope records of mid-Cretaceous Tethyan pelagic
747 sequences from the Umbria – Marche and Belluno Basins (Italy). Newsl. Stratigr. 48,
748 299–323. doi:10.1127/nos/2015/0066

749 Gelin, F., Kok, M.D., De Leeuw, J.W., Sinninghe Damsté, J.S., 1998. Laboratory
750 sulfurisation of the marine microalga Nannochloropsis salina. Organic Geochemistry
751 29, 1837–1848.

752 Gomes, M.L., Hurtgen, M.T., Sageman, B.B., 2016. Biogeochemical sulfur cycling
753 during Cretaceous oceanic anoxic events: A comparison of OAE1a and OAE2.
754 Paleoceanography 1–19. doi:10.1002/(ISSN)1944-9186

755 Hedges, J., & Keil, R. (1995). Sedimentary organic matter preservation: an assessment
756 and speculative synthesis. Marine Chemistry, 49, 81–115.

757 Hedges, J.I., Hu, F.S., Devol, A.H., Hartnett, H.E., Tsamakis, E., Keil, R.G., 1999.
758 Sedimentary organic matter preservation; a test for selective degradation under oxic
759 conditions. American Journal of Science 299, 529–555.

760 Hetzel, A., Böttcher, M.E., Wortmann, U.G., Brumsack, H.-J., 2009. Paleo-redox
761 conditions during OAE 2 reflected in Demerara Rise sediment geochemistry (ODP
762 Leg 207). Palaeogeography, Palaeoclimatology, Palaeoecology 273, 302–328.
763 doi:10.1016/j.palaeo.2008.11.005

764 Jarvis, I., Lignum, J.S., Gröcke, D.R., Jenkyns, H.C., 2011. Black shale deposition,
765 atmospheric CO2 drawdown, and cooling during the Cenomanian-Turonian Oceanic
766 Anoxic Event. Paleoceanography 26. doi:10.1029/2010PA002081

767 Jorgensen, B.B., 1979. A theoretical model of the stable sulfur isotope distribution in
768 marine sediments. Geochimica et Cosmochimica Acta 43, 363–374.

769 Kaplan, I.R., Rittenberg, S.C., 1964. Microbiological fractionation of sulphur isotopes.
770 Journal of General Microbiology 34, 195–212.

771 Keller, G., Adatte, T., Berner, Z., Chellai, E.H., Stueben, D., 2008. Oceanic events and
772 biotic effects of the Cenomanian-Turonian anoxic event, Tarfaya Basin, Morocco.
773 Cretaceous Research 29, 976–994. doi:10.1016/j.cretres.2008.05.020

774 Kolonic, S., Damsté, J., Böttcher, M.E., Kuypers, M.M.M., Kuhnt, W., Scheeder, G.,
775 Wagner, T., beckmann, B., 2002. Geochemical characterization of
776 Cenomanian/Turonian black shales from the Tarfaya Basin (SW Morocco). Journal
777 of Petroleum Geology 25, 325–350.

778 Kolonic, S., Wagner, T., Forster, A., Sinninghe Damsté, J.S., Walsworth-Bell, B., Erba,
779 E., Turgeon, S., Brumsack, H.-J., Chellai, E.H., Tsikos, H., Kuhnt, W., Kuypers,
780 M.M.M., 2005. Black shale deposition on the northwest African Shelf during the
781 Cenomanian/Turonian oceanic anoxic event: Climate coupling and global organic
782 carbon burial. Paleoceanography 20, 1–18. doi:10.1029/2003PA000950

783 Kuypers, M.M.M., Pancost, R.D., Nijenhuis, I.A., Sinninghe Damsté, J.S., 2002.
784 Enhanced productivity led to increased organic carbon burial in the euxinic North
785 Atlantic basin during the late Cenomanian oceanic anoxic event. Paleoceanography
786 17, 1–13. doi:10.1029/2000PA000569

787 Li, X., Gilhooly, W.P., III, Zerkle, A.L., Lyons, T.W., Farquhar, J., Werne, J.P., Varela,
788 R., Scranton, M.I., 2010. Stable sulfur isotopes in the water column of the Cariaco
789 Basin. Geochimica et Cosmochimica Acta 74, 6764–6778.
790 doi:10.1016/j.gca.2010.08.020

791 Little, S.H., Vance, D., Walker-Brown, C., Landing, W.M., 2014. The oceanic mass
792 balance of copper and zinc isotopes, investigated by analysis of their inputs, and
793 outputs to ferromanganese oxide sediments. Geochimica et Cosmochimica Acta 125,
794 673–693. doi:10.1016/j.gca.2013.07.046

795 Louca, S., Crowe, S.A., 2017. Microscale reservoir effects on microbial sulfur isotope
796 fractionation. Geochimica et Cosmochimica Acta 203, 117–139.
797 doi:10.1016/j.gca.2017.01.007

798 Lowenstein, T.K., Hardie, L.A., Timofeeff, M.N., Demicco, R.V., 2003. Secular
799 variation in seawater chemistry and the origin of calcium chloride basinal brines.
800 Geology 31, 857–860. doi:10.1130/G19728R.1

801 Lyons, T.W., Werne, J.P., Hollander, D.J., Murray, R.W., 2003. Contrasting sulfur
802 geochemistry and Fe/Al and Mo/Al ratios across the last oxic-to-anoxic transition in
803 the Cariaco Basin, Venezuela. Chemical Geology 195, 131–157. doi:10.1016/S0009-
804 2541(02)00392-3

805 Middelburg, J.J., Levin, L.A., 2009. Coastal hypoxia and sediment biogeochemistry.
806 Biogeosciences 6, 1273–1293. doi:10.5194/bg-6-1273-2009

807 Ostrander, C.M., Owens, J.D., Nielsen, S.G., 2017. Constraining the rate of oceanic
808 deoxygenation leading up to a Cretaceous Oceanic Anoxic Event (OAE-2: ~94 Ma).
809 Science Advances 3, 1–6.

810 Owens, J.D., Gill, B.C., Jenkyns, H.C., 2013. Sulfur isotopes track the global extent and
811 dynamics of euxinia during Cretaceous Oceanic Anoxic Event 2. Proceedings of the
812 National Academy of Sciences 110, 18407-18412.

Owens, J.D., Lyons, T.W., Li, X., Macleod, K.G., 2012. Iron isotope and trace metal records of iron cycling in the proto North Atlantic during the Cenomanian Turonian oceanic anoxic event (OAE 2). Paleoceanography. doi:10.1029/2012PA002328

Owens, J.D., Lyons, T.W., Lowery, C.M., 2018. Quantifying the missing sink for global organic carbon burial during a Cretaceous oceanic anoxic event. Earth and Planetary Science Letters 499, 83–94. doi:10.1016/j.epsl.2018.07.021

Owens, J.D., Reinhard, C.T., Rohrssen, M., Love, G.D., Lyons, T.W., 2016. Empirical links between trace metal cycling and marine microbial ecology during a large perturbation to Earth's carbon cycle. Earth and Planetary Science Letters 449, 407–417. doi:10.1016/j.epsl.2016.05.046

Pohlabeln, A.M., Gomez-Saez, G.V., Noriega-Ortega, B.E., Dittmar, T., 2017. Experimental Evidence for Abiotic Sulfurization of Marine Dissolved Organic Matter. Frontiers in Marine Sci. 4, 265. doi:10.3389/fmars.2017.00364

Poulton, S., Canfield, D., 2005. Development of a sequential extraction procedure for iron: implications for iron partitioning in continentally derived particulates. Chemical Geology 214, 209–221. doi:10.1016/j.chemgeo.2004.09.003

Poulton, S.W., Henkel, S., März, C., Urquhart, H., Flögel, S., Kasten, S., Sinninghe Damsté, J.S., Wagner, T., 2015. A continental-weathering control on orbitally driven redox-nutrient cycling during Cretaceous Oceanic Anoxic Event 2. Geology 43, 963–966. doi:10.1130/G36837.1

Poulton, S.W., Raiswell, R., 2002. The low-temperature geochemical cycle of iron: From continental fluxes to marine sediment deposition. American Journal of Science 302, 774–805. doi:10.2475/ajs.302.9.774

Raiswell, R., Canfield, D.E., 1996. Rates of reaction between silicate iron and dissolved sulfide in Peru Margin sediments. Geochimica et Cosmochimica Acta 60, 2777–2787.

Raven, M.R., Fike, D.A., Gomes, M.L., Webb, S.M., Bradley, A.S., McClelland, H.-L.O., 2018. Organic carbon burial during OAE2 driven by changes in the locus of organic matter sulfurization. Nature Communications 9, 3409. doi:10.1038/s41467-018-05943-6

Raven, M.R., Sessions, A.L., Adkins, J.F., Thunell, R.C., 2016a. Rapid organic matter sulfurization in sinking particles from the Cariaco Basin water column. Geochimica et Cosmochimica Acta 190, 175–190. doi:10.1016/j.gca.2016.06.030

Raven, M.R., Sessions, A.L., Fischer, W.W., Adkins, J.F., 2016b. Sedimentary pyrite δ 34 S differs from porewater sulfide in Santa Barbara Basin: Proposed role of organic sulfur. Geochimica et Cosmochimica Acta 186, 120–134. doi:10.1016/j.gca.2016.04.037

Sageman, B.B., Meyers, S.R., Arthur, M.A., 2006. Orbital time scale and new C-isotope record for Cenomanian-Turonian boundary stratotype. Geology 34, 125–4. doi:10.1130/G22074.1

853 Sinninghe Damsté, J.S., Köster, J., 1998. A euxinic southern North Atlantic Ocean during
854 the Cenomanian/Turonian oceanic anoxic event. Geochimica et Cosmochimica Acta
855 158, 165–173.

856 Vairavamurthy, A., 1998. Using X-ray absorption to probe sulfur oxidation states in
857 complex molecules. Spectrochimica Acta Part A 54, 2009–2017. doi:10.1016/S1386-
858 1425(98)00153-X

859 van Dongen, B.E., Schouten, S., Baas, M., Geenevasen, J.A.J., Sinninghe Damsté, J.S.,
860 2003. An experimental study of the low-temperature sulfurization of carbohydrates.
861 Organic Geochemistry 34, 1129–1144. doi:10.1016/S0146-6380(03)00060-3

862 Wan, M., Schröder, C., Peiffer, S., 2017. Fe (III): S (-II) Concentration Ratio Controls the
863 Pathway and the Kinetics of Pyrite Formation during Sulfidation of Ferric
864 Hydroxides. Geochimica et Cosmochimica Acta. doi:10.1016/j.gca.2017.08.036

865 Webb, S.M., 2005. SIXpack: a graphical user interface for XAS analysis using IFEFFIT.
866 Phys. Scr. 2005, 1011. doi:10.1238/Physica.Topical.115a01011

867 Wenk, C.B., Wing, B.A., Halevy, I., 2017. Electron carriers in microbial sulfate reduction
868 inferred from experimental and environmental sulfur isotope fractionations. The
869 ISME Journal 12, 1–13. doi:10.1038/ismej.2017.185

870 Werne, J., Lyons, T., Hollander, D., Schouten, S., Hopmans, E., & Damste, J. (2008).
871 Investigating pathways of diagenetic organic matter sulfurization using compound-
872 specific sulfur isotope analysis. Geochimica Et Cosmochimica Acta, 72, 3489–3502.

873 Werne, J.P., Lyons, T.W., Hollander, D.J., Chemical, M.F., Sinninghe Damsté, J.S.,
874 2003. Reduced sulfur in euxinic sediments of the Cariaco Basin: sulfur isotope
875 constraints on organic sulfur formation. Geochimica et Cosmochimica Acta 195,
876 159–179. doi:10.1016/S0009-2541(02)00393-5

877